https://doi.org/10.5194/egusphere-2024-3196
Preprint. Discussion started: 8 November 2024

Quantifying degradation of the Imja Lake moraine dam with fused InSAR and SAR feature tracking time series

George Brencher[1], Scott T. Henderson[2,3], David E. Shean[1]

[1]University of Washington Department of Civil and Environmental Engineering, 1400 NE Campus Parkway, Seattle, WA 98195, USA
[2]University of Washington Department of Earth and Space Sciences, 1707 NE Grant Lane, Seattle, WA 98195, USA
[3]University of Washington eScience Institute, 1410 NE Campus Parkway, Seattle, WA 98195, USA

Correspondence to: George Brencher (gbrench@uw.edu)

Abstract. Glacial lake outburst flood (GLOF) hazards are often tied to the structural properties of the moraines that dam glacial lakes. Traditional investigations of moraine dam structure and degradation involve costly and logistically challenging in-situ geophysical and repeat topographic surveys, which can only be performed for a small number of sites. We developed a scalable satellite remote sensing approach using interferometric synthetic aperture radar (InSAR), InSAR coherence, and SAR feature tracking to precisely measure moraine dam surface displacement and map the extent of buried ice. We combined time series from ascending and descending Sentinel-1 orbits to investigate vertical and horizontal surface displacement from 2017-2024 with ~12-day temporal sampling.

We applied our approach to quantify degradation of the Imja Lake moraine dam in the Everest Region of Nepal. We find that a 0.3 km^2 area of the moraine dam has cumulatively subsided ~90 cm over the 7-year study period. Seasonal change in InSAR coherence provides evidence for buried ice throughout the moraine dam. We observe consistent downward and eastward displacement throughout the colder months, which we attribute to ice flow. The magnitude of downward vertical surface velocity increases in the warmer months, likely due to melting of buried ice. Our observations provide new insights into the timing and magnitude of the processes that control moraine dam development and evolution, with broader implications for regional GLOF hazard assessment and mitigation.

1 Introduction

Glaciers in High Mountain Asia (HMA), Earth's largest glacierized region outside the poles, are expected to lose between ~29 and 67% of their total mass by the end of the century (Hock et al., 2019; Rounce et al., 2020). Worldwide, glacier thinning and retreat is associated with an increase in the formation of glacial lakes dammed by unstable ice-cored moraines (Shugar et al., 2020). These lakes constitute a significant hazard, as they can drain in sudden, catastrophic glacier lake outburst flood (GLOF) events that flood downstream valleys and result in loss of life and damage to infrastructure (Mool et al., 2011; Riaz et al., 2014; Carrivick & Tweed, 2016). For example, the September 2023 GLOF event in Sikkim, India, destroyed the Teesta III

https://doi.org/10.5194/egusphere-2024-3196
Preprint. Discussion started: 8 November 2024

hydroelectric dam, washed away 15 bridges, stranded 3,000 tourists, and left at least 74 dead with more missing (Ali Badal, 2023; Choudhury & Hussain, 2023; Kumar & Travelli, 2023; Sebastian, 2023).

Effective management of GLOF hazards involves 1) identification and monitoring of glacial lakes that pose a significant hazard, and 2) mitigation of this hazard before GLOFs occur, potentially through engineering solutions. The former has been primarily accomplished through hazard assessments ranging from a single lake (e.g. Budhathoki et al., 1970; Rana et al., 2000; Wang et al., 2018; Sattar et al., 2021) to regional scale (e.g. Mool et al., 2011; Wang et al., 2012; Fujita et al., 2013; Allen et al., 2016; Rounce et al., 2017). These hazard assessments frequently consider moraine dam stability, potential GLOF triggering events, and potential downstream impact (Rounce et al., 2016). GLOFs can be triggered by rockfall, landslides, avalanches, glacier calving, and failure of the moraine dam (Costa & Schuster, 1988; Neupane et al., 2019). Where moraine dam instability is not a direct trigger of GLOFs, melting of buried ice can increase lake area, reduce width and height of dams, and provide potential pathways for seepage and piping (Richardson & Reynolds, 2000a; Emmer & Cochachin, 2013). As such, evolution of moraine dams may substantially impact GLOF likelihood.

Engineering solutions for mitigating GLOF hazards may involve lowering lake levels via artificial cuts and tunnels, moraine dam reinforcement and modification, and installation of monitoring equipment and early warning systems (Hanisch et al., 2000; Emmer et al., 2018; Huggel et al., 2020). Artificially draining glacial lakes is “technically challenging, labor intensive, costly, and potentially risky” (UNDP, 2012). Prior to lake lowering and moraine dam modification, in-situ geophysical surveys have been conducted to map internal moraine structure and identify the location of buried ice (Somos-Valenzuela et al., 2013).

As glacial lakes, moraine dams, and the surrounding landscape change over time (Huggel et al., 2010; Shugar & Clague, 2011; Kellerer-pirklbauer et al., 2012; Ravanel et al., 2018), hazard assessment and mitigation tasks require repeated observations (Fujita et al., 2009; Rounce et al., 2017; Emmer et al., 2018). Satellite remote sensing has been used to create glacial lake inventories, track glacial lake development (e.g. Fujita et al., 2009; Nie et al., 2018; Shugar et al., 2020), and recently, to monitor glacial lake dam and bank evolution (Haritashya et al., 2018; Scapozza et al., 2019; Yang et al., 2022; Jiang et al., 2023; Yang et al., 2023; Yu et al., 2024). These remote measurements of surface displacement can be used to assess moraine dam stability, infer moraine dam structure, and quantify change in moraine dam topography, providing critical information for GLOF hazard assessments and potentially guiding prioritization for in-situ surveys and hazard mitigation strategies.

Here, we present a new method that leverages time series of satellite synthetic aperture radar (SAR) images to precisely measure moraine dam surface movement over the past decade. We used this new approach to characterize moraine dam kinematics and improve understanding of processes contributing to the Imja Lake moraine dam evolution in the Everest region of Nepal (Fig. 1).

https://doi.org/10.5194/egusphere-2024-3196
Preprint. Discussion started: 8 November 2024

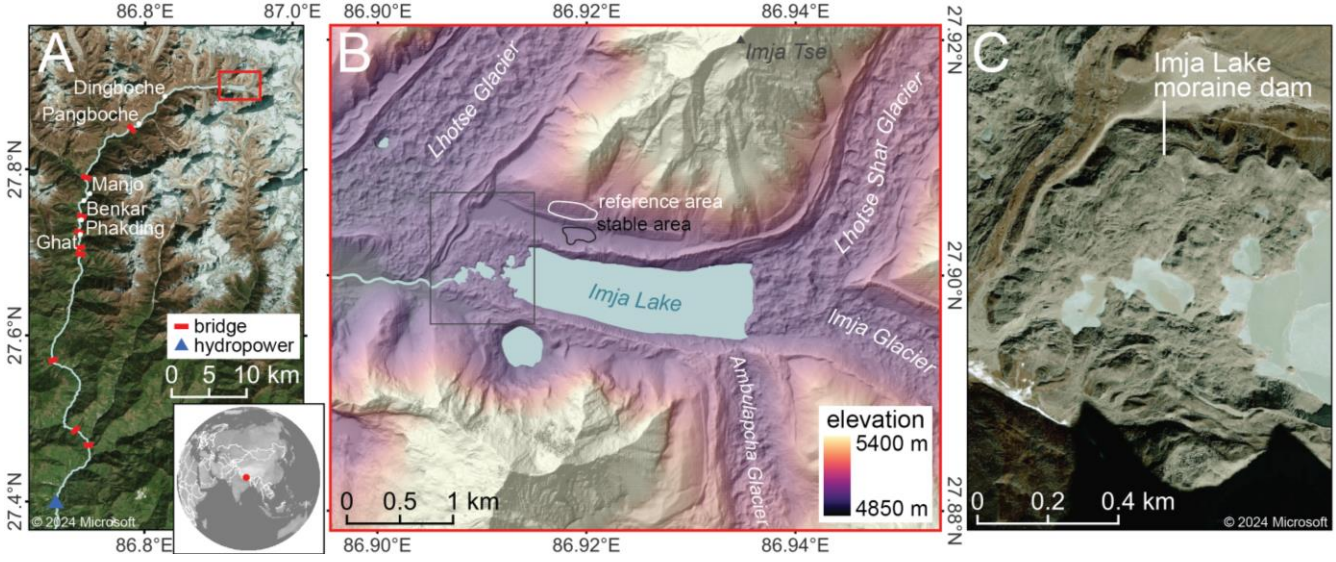

Figure 1: Maps showing Imja Lake moraine dam. A) Bing satellite basemap showing the area downstream of Imja Lake, including settlements and infrastructure along the Dhudh Kohsi river. B) Color-shaded relief map from median composite of EarthDEM strips acquired during the 2014-2019 period (Porter et al., 2022). C) © Microsoft satellite basemap showing detail of the Imja Lake moraine dam. Microsoft product screen shots reprinted with permission from Microsoft Corporation.

1.1 Moraine dam evolution

Ice-cored moraines are found globally in modern glacier forelands (Østrem, 1959). These features, which range in size from the decameter to kilometer scale, are typically formed at glacier margins when ice overlain by insulating debris cover is disconnected from the active glacier through differential ablation (Østrem, 1959; Kjær & Krüger, 2001; Lukas, 2011). Ice-cored moraines often impound meltwater to form proglacial glacial lakes, becoming moraine dams.

Once cut off from the active upstream glacier, ice-cored moraine dam degradation proceeds through a group of related processes, which change the topographic and structural characteristics of the moraine dams over time. Understanding these mechanisms is important for both method development and interpretation of surface displacement measurements from remote sensing observations. Several processes contribute to degradation of ice-cored moraines, including 1) downwasting, 2) thermokarst, 3) backwasting, and 4) debris reworking.

Downwasting, or vertical subsidence of ice-cored features, occurs due to melting and sublimation of buried ice (Lukas, 2011). Downwasting rates have been observed to vary between 0.003 and 4.8 m/yr, and spatiotemporal variability is correlated with mean annual temperature and debris thickness (Irvine-Fynn et al., 2011). The downwasting rate of ice-cored moraine dams may have significant implications for GLOF hazards, as it relates directly to changes in the freeboard height of the dam and changes the shape of the shoreline, leading to lake expansion.

https://doi.org/10.5194/egusphere-2024-3196
Preprint. Discussion started: 8 November 2024

Thermokarst occurs where melting of glacial ice or ground ice beneath unconsolidated sediments creates pseudokarst landforms, including kettles and sinkholes (Healy, 1975). Thermokarst landforms may contribute to rapid surface lowering as melting of buried ice is accelerated by the presence of liquid water (Richardson & Reynolds, 2000b). Remnant glacial structures including water and debris-filled crevasses likely exert a primary control over thermokarst landform location (Richardson & Reynolds, 2000b).

Backwasting, or lateral retreat of near-vertical ice walls and ice-cored slopes, is the dominant ice loss mechanism for most ice-cored moraines (Krüger & Kjær, 2000; Lukas, 2011). Unlike downwasting, backwasting rates are controlled by incoming shortwave radiation rather than debris thickness or mean annual temperature (Johnson, 1971; Schomacker, 2008). Schomacker (2008) compiled measurements of backwasting rates between 0.65 and 24 m/yr for fourteen features across six Randolph Glacier Inventory regions.

Lakes act as heat and sediment reservoirs, and ice-cored dam degradation can be accelerated by interaction with the glacial lake and surface ponds (Johnson, 1971; Driscoll, 1980; Pickard, 1983; Watanabe et al., 1995). Removal and redistribution of moraine dam debris via debris flows and fluvial transport expose ice-cored slopes to backwasting, change the spatial pattern of debris insulation, and remove debris from the system, which can affect structural stability (Lukas et al., 2005; Schomacker & Kjær, 2008). Debris flows cause backwasting of the shoreline away from the lake, decreasing moraine width, and increasing lake area (Watanabe et al., 1995). In addition to debris flows, rotational failures of moraine material associated with melt of ice cores have also been observed (Richardson & Reynolds, 2000b). Sediment and ice mass movements can also indirectly contribute to GLOF risk by changing the shape and structure of moraine dams, and/or directly triggering GLOFs by creating waves that overtop the moraine dam.

1.2 Remote sensing of moraine dam degradation

We propose a novel approach to combine C-band (~5.6 cm wavelength) InSAR and SAR feature tracking to measure displacement of moraine dams and distinguish between various physical degradation processes. C-band SAR can operate during both day or night, penetrate through clouds, and penetrate thin, dry snow (Bürgmann et al., 2000; Sun et al., 2015). Both InSAR and feature tracking provide measurements of surface motion along the radar line-of-sight (LOS).

InSAR relates the phase offset from successive SAR acquisitions to surface displacement (Bürgmann et al., 2000; Rosen et al., 2000). InSAR has frequently been applied to measure displacement of ice-rich features with mm-level accuracy, including glaciers (Massonnet & Feigl, 1998; Rosen et al., 2000), rock glaciers (Bertone et al., 2022), and permafrost (Zhang et al., 2022). Recently, InSAR has also been applied to quantify surface movement of glacial lake dams (Scapozza et al., 2019; Yang et al., 2022; Jiang et al., 2023; Yang et al., 2023; Yu et al., 2024).

https://doi.org/10.5194/egusphere-2024-3196
Preprint. Discussion started: 8 November 2024

While InSAR offers unparalleled precision, several factors can reduce measurement accuracy, including atmospheric noise, layover and radar shadow. InSAR requires 1) coherent surface change with similar scatterer characteristics between radar acquisitions, and 2) displacement between adjacent pixels of less than half the radar wavelength (2.8 cm for C-band) (Itoh, 1982; Handwerger et al., 2015). While errors caused by atmospheric conditions and acquisition geometry can be avoided or corrected, errors caused by rapid surface change may cause underestimation of true LOS surface velocity. InSAR coherence, a unitless measure of the "sameness" of surface scatterers between acquisitions, can be used to discriminate between reliable and unreliable InSAR measurements (e.g. Schmidt & Bürgmann, 2003). InSAR coherence can also be used to identify significant change in surface characteristics, and low coherence has been used to map the extent of desert erosion (e.g. Cabré et al., 2020), landslides (e.g. Ohki et al., 2020), flooding (e.g. Chini et al., 2019), and debris-covered glaciers (e.g. Lippl et al., 2018).

Feature tracking offers an alternative method to retrieve surface displacement measurements from SAR data when InSAR is not possible due to loss of coherence. Feature tracking involves 2D cross-correlation of backscatter amplitude values in successive radar images to measure offsets in the range (across-track) and azimuth (along-track) directions. This technique has been used to measure glacier surface velocity (e.g. Fahnestock et al., 1993; Strozzi et al., 2002, 2008; Fahnestock et al., 2016) and fast-moving features surrounding glacial lakes (Scapozza et al., 2019; Yang et al., 2022). While feature-tracking measurements offer lower resolution and precision than InSAR measurements, they are more robust to large surface displacements and rapid surface change (Joughin, 2002, Zheng et al., 2023).

By combining InSAR and feature tracking measurements, we can leverage the strengths of both methods to provide a more complete record and understanding of moraine dam kinematics. This approach captures large seasonal variations, including slow cold-season displacement with InSAR and rapid warm-season surface change with feature tracking. Previous studies combined InSAR and feature tracking to produce self-consistent surface displacement maps over large ice sheets and ice caps, where surface velocity is often too fast for InSAR alone (e.g., Joughin, 2002; Liu et al., 2007; Sánchez-Gámez & Navarro, 2017; Joughin et al., 2018). To our knowledge, no studies have combined these techniques to measure year-round surface displacement of ice-cored moraine features, where we expect seasonal variability in surface melt rates and associated debris reworking.

2 Imja Lake Study Site

Imja Lake is a ~2.8 by 0.6 km glacial lake covering ~1.6 km^2 in the Everest region of Nepal (Fig. 1). Imja Lake is impounded on its north and south sides by lateral moraines, above which rise the steep slopes of adjacent mountain peaks: Imja Tse to the north and Ombigaichen to the south. To the east, the ~860 m wide calving front of the Lhoste Shar and Imja Glaciers terminate in the lake. Imja Lake formed in the early 1970s as supraglacial lakes on the stagnant, debris-covered tongue of the Imja

https://doi.org/10.5194/egusphere-2024-3196
Preprint. Discussion started: 8 November 2024

Glacier coalesced. It expanded at a roughly linear rate of 0.02 km^2/yr to its current size throughout the ensuing decades (Watanabe et al., 2009).

To the west, Imja Lake is impounded by an ice-cored terminal moraine covering 0.62 km^2. The Imja Lake moraine dam (hereafter, the moraine dam) has a low-relief hummocky surface with ridges and furrows, ponds, and ice cliffs, with a mean elevation of 4982 m (orthometric height above the EGM2008 geoid). The lake drains over the moraine via a series of linked ponds. An artificial drainage channel was constructed downstream of the western pond in 2016 (UNDP, 2012; Khadra, 2016). The moraine dam has an enclosed concave-up surface, and broadly slopes down toward the lake and surface ponds (Supplemental Fig. 1).

Geophysical studies using ground-penetrating radar (GPR) and electrical resistivity tomography (ERT) have examined the subsurface structure of the moraine dam and documented the extent, depth, and thickness of buried ice (Hambrey et al., 2008; Somos-Valenzuela et al., 2012; Dahal et al., 2018). Hambrey et al. (2008) used both GPR and ERT to document buried glacier ice tens of meters thick (over 40 meters in places) overlain by up to 20 m of debris along the eastern portion of the moraine. Similar profiles along western portion of the moraine revealed water-saturated debris but no evidence of buried glacial ice. Somos-Valenzuela et al., (2012) found consistent evidence for buried ice throughout 13 GPR transects across the moraine dam, ranging in bottom depth from 0-65 m. The deepest ice bottom depths (40-60 m) were documented on the northeast moraine dam, while shallower ice bottom depths (20-40 m) were documented around the southwest margin of the moraine dam, near the outlet. Dahal et al., (2018) conducted a dense ERT survey of the area surrounding the moraine dam outlet to the southwest, finding evidence for discontinuous blocks of glacier ice at depths varying from 0-20 m.

Two studies have quantified Imja Lake moraine dam degradation rates using in situ measurements obtained with traditional and GNSS surveying techniques. Watanabe et al., (1995) measured the position of five painted boulders in November 1989 and October 1994 and documented cumulative vertical displacements of -0.3 to -13.5 m with a mean of -4.8 m over the 5-year period (corresponding to vertical velocity of -0.06 to -2.70 m/yr and mean of -1.0 m/yr). The boulders also moved horizontally in the west-southwest direction, with one boulder moving up to 12.7 m, corresponding to a horizontal velocity of 2.58 m/yr. Fujita et al., (2009) performed topographic surveys using a theodolite in November 2001 and GPS receivers in April 2002 and October 2007. They created digital elevation models (DEMs) with 1 m posting for each survey and differenced to obtain surface displacement measurements. The authors report cumulative vertical displacements for the “left bank” and “right bank” of -1.63 ± 1.71 m and -1.97 ± 1.67 m (mean ± 1-sigma), respectively, with vertical velocity of -0.06 to -1.03 m/yr for the 6-year period from 2001 to 2007. Velocity was generally higher in the northeast area of the moraine dam. The authors also describe horizontal displacement of painted stones of less than 1 m between 2001 and 2007.

https://doi.org/10.5194/egusphere-2024-3196
Preprint. Discussion started: 8 November 2024

Haritashya et al. (2018) measured moraine dam displacement by differencing the 30-m Shuttle Radar Topographic Mission Global 1 (SRTM-GL1) DEM acquired in February 2000 with a 2-m WorldView stereo DEM acquired in February 2016. Mean vertical displacement over the moraine dam was less than -0.5 m/yr, with a maximum displacement of -1.9 m/yr and uncertainty of 0.7 m/yr.

3 Data

We downloaded all available Copernicus Sentinel-1 C-band single-look complex (SLC) SAR images collected over the study site from January 1, 2017 through March 1, 2024. The revisit time for this period was generally 12 days, and we did not include data before 2017 due to longer gaps between acquisitions. All images were acquired in interferometric wide (IW) swath mode with vertical co-polarization (VV) along ascending (satellite moving north and looking east) relative orbit 12 and descending (satellite moving south and looking west) relative orbit 121. To minimize download time and storage, we limited processing to SLC bursts covering our study site, with a total of 214 ascending burst acquisitions (Burst ID 012_023790_IW1) and 227 descending burst acquisitions (Burst ID 121_258661_IW2). Burst dimensions are ~20 km in azimuth by ~85 km in range with pixel spacing of 14.1 m in azimuth and 2.3 m in range (Supplemental Fig. 2).

We used the 2022_1 release of the 30-m Copernicus GLO-30 DEM (European Space Agency, 2021) to remove the topographic component of the phase and geocode the SAR data products. The GLO-30 DEM product has an absolute vertical accuracy (LE90) of <4 m and an absolute horizontal accuracy (CE90) of <6 m (NSDDA, 1998; European Space Agency, 2022).

We downloaded daily 2-m air temperature and total precipitation data from the Pyramid Weather Station (UCAR/NCAR-Earth Observing Laboratory et al., 2011), which is located ~11 km northwest of the Imja Lake moraine dam at an elevation of 4951 m, about 30 m lower than the elevation of the moraine dam. We aggregated available daily measurements between October 1, 2002 to December 31, 2009 to derive monthly climatology (mean, minimum, maximum and standard deviation) for the ~7-year period.

4 Methods

4.1 SAR data processing

To extract surface displacement information from the Sentinel-1 SLC products, we generated both interferograms and feature tracking offsets using the Hybrid Pluggable Processing Pipeline (HyP3) ISCE2 Plugin (Hogenson et al., 2020), which enables batch processing with the Jet Propulsion Laboratory InSAR Scientific Computing Environment (ISCE) software (Rosen et al., 2012; version 2.6.3).

https://doi.org/10.5194/egusphere-2024-3196
Preprint. Discussion started: 8 November 2024

The insar_tops_burst workflow was used to process interferograms with five looks in range and one look in azimuth, geocoded to 20 m square pixels (Supplemental Fig. 2). To form redundant networks of ascending and descending interferograms, we created interferograms for each burst acquisition using the three nearest burst acquisitions in time. In total, we processed 636 ascending burst interferograms and 675 descending burst interferograms (Table 1).

We selected a local "reference area" and "stable area" (Fig. 1) with high mean InSAR coherence for the entire study period to remove atmospheric noise and assess measurement accuracy. The reference area spanned ~0.06 km^2 (~144 pixels) approximately ~250 m northwest of the moraine dam (Fig. 1). We computed and subtracted the median apparent displacement over the reference area from each interferogram.

We coregistered all SLCs and performed feature tracking on the slant range SLC products with no multilooking using a modified version of the insar_tops_burst workflow and the 'dense ampcor' ISCE2 feature tracking routine. We experimented with a variety of kernel sizes before selecting dimensions of 10 pixels in azimuth and 60 pixels in range, or 141 by 138 m. This kernel size was selected to avoid noise caused by poor matches from small kernels and potential underestimation of displacement by large kernels that included stable areas outside the moraine dam. The skip size was set to 4 pixels in azimuth and 20 pixels in range, or 56 m by 46 m, and bilinear interpolation was used to fill gaps between offset measurements. Search window size was set to 10 pixels in azimuth and 30 pixels in range, or 141 m by 69 m, much larger than the expected surface displacement of the moraine dam.

Assuming perfect SLC coregistration and a conservative feature-tracking precision of 0.2 pixels (Fialko & Simons, 2001; Strozzi et al., 2002), the theoretical accuracy of our feature tracking measurements is 2.82 m in azimuth and 0.46 m in range. Given the expected mean surface velocity of <1 m per year for the moraine dam (Fujita et al., 2009), we generated feature tracking offsets with multi-year temporal baselines to maximize displacement between acquisitions. As longer temporal baselines could result in degraded quality due to significant changes in surface scatterer characteristics, we generated offsets for all possible feature tracking image pairs with temporal baselines of 4, 5, and 6 years (Table 1). In total, we generated 192 ascending and 210 descending feature tracking offset maps with corresponding signal-to-noise ratio (SNR) maps.

Table 1. Summary of InSAR and feature tracking datasets.

orbit	acquisitions	dataset	pair count	mean temporal baseline	temporal baseline range
ascending track 12, Burst ID 012_023790_IW1	214	InSAR	636	24.3 days	12-48 days
		feature tracking	192	4.7 years	4-6 years
descending track 121, Burst ID 121_258661_IW2	227	InSAR	675	23.0 days	6-60 days
		feature tracking	210	4.7 years	4-6 years

https://doi.org/10.5194/egusphere-2024-3196
Preprint. Discussion started: 8 November 2024

4.2 Time series inversion

Since both InSAR interferograms and feature tracking offset maps in the range direction are measurements of displacement along the satellite line-of-sight, these measurements can be combined to create more accurate estimates of surface displacement over time. We used the Miami INsar Time-series software in PYthon (MintPy) package (Yunjun et al., 2019) to prepare cumulative LOS displacement time series from all InSAR and feature tracking observations for each relative orbit.

To avoid cumulative displacement errors caused by poor feature tracking matches, we aggregated the feature tracking offset products and prepared a single median velocity product for each relative orbit. These median velocity products were then used to constrain the cumulative displacement solution from the network of InSAR interferograms from the same relative orbit.

Several preprocessing steps were required to produce the median feature tracking velocity products for each relative orbit. We first converted all feature tracking offsets in range from pixels to C-band phase in radians. We then masked all pixels with signal-to-noise ratio lower than 8 to remove unreliable measurements. Next, we removed any pixels with apparent surface displacement of more than 10 m, which exceed the expected cumulative displacement of the moraine dam during the 6-year study period (Hambrey et al., 2008; Fujita et al., 2009; Haritashya et al., 2018). We then calculated the median surface displacement in range observed in the reference area and subtracted it from each offset map to mitigate potential co-registration bias. At this point we divided each feature tracking offset map in range by its temporal baseline and computed a per-pixel median rate for the entire time series stack, resulting in a single median velocity product for each relative orbit. We masked any pixels with less than 10 feature-tracking observations or a mean InSAR coherence greater than 0.85 during late summer (day of year 220-280, the lowest coherence period, Fig. 2), as the InSAR measurements alone should provide accurate displacement time series for those pixels. We also computed the per-pixel normalized median absolute deviation (NMAD, a robust estimator equal to standard deviation for a normal distribution) of the feature tracking offset maps to assess variability due to real changes and measurement error.

Prior to time series inversion, we removed interferograms with mean coherence of less than 0.6 over the moraine dam, unless they were required to form a continuous network. This filter removed interferograms impacted by intermittent snow accumulation, large perpendicular baselines (typically >200 m), or large surface change over the temporal baseline. We scaled the per-pixel median feature-tracking velocity products to estimate the cumulative displacement over the entire study period for the inversion. The network of per-pixel displacement measurements was then inverted using this cumulative displacement and phase variance as a weight (Yunjun et al., 2019). Finally, we delineated a ‘moving area’ over the moraine dam for pixels with mean velocity of ~1 cm/yr above the background noise level in the ascending and descending cumulative displacement time series.

https://doi.org/10.5194/egusphere-2024-3196
Preprint. Discussion started: 8 November 2024

4.3 Surface displacement from LOS decomposition

Given two cumulative displacement measurements over the moraine dam, each with a different LOS from different relative orbits, we can solve for two components of the 3D surface displacement vector (Wright et al., 2004; Fuhrmann & Garthwaite, 2019). Since the mean LOS incidence angle at the site is 35.8° for the ascending burst and 37.8° for the descending burst, and the mean LOS azimuth (defined clockwise from north) is 79.3° for the ascending burst and 280.5° for the descending burst, we chose to solve for the vertical (up/down) and horizontal (east/west) surface displacement components. We assume that any north/south displacement would be negligible when projected into the available line-of-sight vectors.

The LOS unit vector ($\hat{l}$) of each pixel can be defined as:

$$\hat{l} = \cos(\gamma)\sin(\theta)\,\hat{n} + \sin(\gamma)\sin(\theta)\,\hat{e} - \cos(\theta)\,\hat{z}\,, \quad (1)$$

for ascending ($\hat{l}_{asc}$) and descending ($\hat{l}_{des}$) geometry, where γ is the LOS azimuth angle, θ is the LOS incidence angle defined relative to surface-normal direction, and $\hat{n}$, $\hat{e}$ and $\hat{z}$ represent the north, east, and up axes, respectively, which define the up/down $\hat{l}_{ud} = 0\hat{n} + 0\hat{e} + 1\hat{z}$ and east/west $\hat{l}_{ew} = 0\hat{n} + 1\hat{e} + 0\hat{z}$ unit vectors.

If we assume that the observed cumulative ascending ($d_{asc}(t)$) and descending ($d_{des}(t)$) displacement at time t is only sensitive to the up/down ($d_{ud}(t)$) and east/west ($d_{ew}(t)$) surface displacement components, we obtain the following equations:

$$d_{asc(t)} = \hat{l}_{asc} \cdot \hat{l}_{ud} * d_{ud}(t) + \hat{l}_{asc} \cdot \hat{l}_{ew} * d_{ew}(t)\,, \quad (2)$$

$$d_{des(t)} = \hat{l}_{des} \cdot \hat{l}_{ud} * d_{ud}(t) + \hat{l}_{des} \cdot \hat{l}_{ew} * d_{ew}(t)\,, \quad (3)$$

We can then rearrange these equations to solve for the up/down and east/west displacement components:

$$d_{ud}(t) = \frac{\hat{l}_{asc}\cdot\hat{l}_{ew} * d_{des}(t) - \hat{l}_{des}\cdot\hat{l}_{ew} * d_{asc}(t)}{\hat{l}_{asc}\cdot\hat{l}_{ew} * \hat{l}_{des}\cdot\hat{l}_{ud} - \hat{l}_{des}\cdot\hat{l}_{ew} * \hat{l}_{asc}\cdot\hat{l}_{ud}}\,, \quad (4)$$

$$d_{ew}(t) = \frac{\hat{l}_{asc}\cdot\hat{l}_{ud} * d_{ud}(t) - d_{asc}(t)}{\hat{l}_{asc}\cdot\hat{l}_{ew}}\,, \quad (5)$$

To accomplish this, we interpolated the descending orbit cumulative displacement time series to match the acquisition dates of the ascending orbit cumulative displacement time series, and then solved for the vertical and east/west displacement at every pixel at each ascending acquisition time.

https://doi.org/10.5194/egusphere-2024-3196
Preprint. Discussion started: 8 November 2024

4.4 Surface velocity

We computed the vertical and east/west surface velocity by dividing observed cumulative displacement by the time between acquisition dates. We aggregated these velocity component time series to compute the per-pixel monthly median values over the entire study period.

4.5 Buried ice extent

To identify and map areas of buried ice, we calculated a winter coherence map using the per-pixel median coherence for all 12-day temporal baseline observations in winter to early spring (day of year 0 – 100), and a summer coherence map using the per-pixel median coherence for observations in late summer (day of year 220-280). We attribute large observed seasonal decreases in InSAR coherence to surface changes caused by melting of buried ice during warm months.

5 Results

5.1 InSAR coherence

We examined mean InSAR coherence from all pairs on both the ascending and descending orbits over the Imja Lake moraine dam during the full 2017-2024 study period. The pair temporal baseline strongly controlled InSAR coherence over the moraine dam moving area (Fig. 2E, F), with shorter temporal baselines (i.e., 12 days) offering higher mean coherence than longer temporal baselines (i.e., 36-60 days). Over the stable area, we observed no obvious relationship between temporal baseline and coherence (Fig. 2G, H). Descending orbit coherence was on average slightly higher (mean 0.80) than ascending orbit coherence (0.74) over the moraine dam moving area for 12-day temporal baseline interferograms.

We observed a systematic seasonal cycle in InSAR coherence values over the moraine dam moving area. Coherence remained largely stable from the beginning of the year until early June. For 12-day temporal baseline interferograms, mean coherence declined by approximately 0.3 from June through mid-September. Coherence then increased from mid-September through mid-November. This seasonal decrease in coherence lags about 60 days behind the timing of positive mean daily maximum temperatures at the nearby Pyramid Station (Fig. 2E, F). No significant seasonal coherence change was observed over the stable area (Fig. 2G, H).

https://doi.org/10.5194/egusphere-2024-3196
Preprint. Discussion started: 8 November 2024

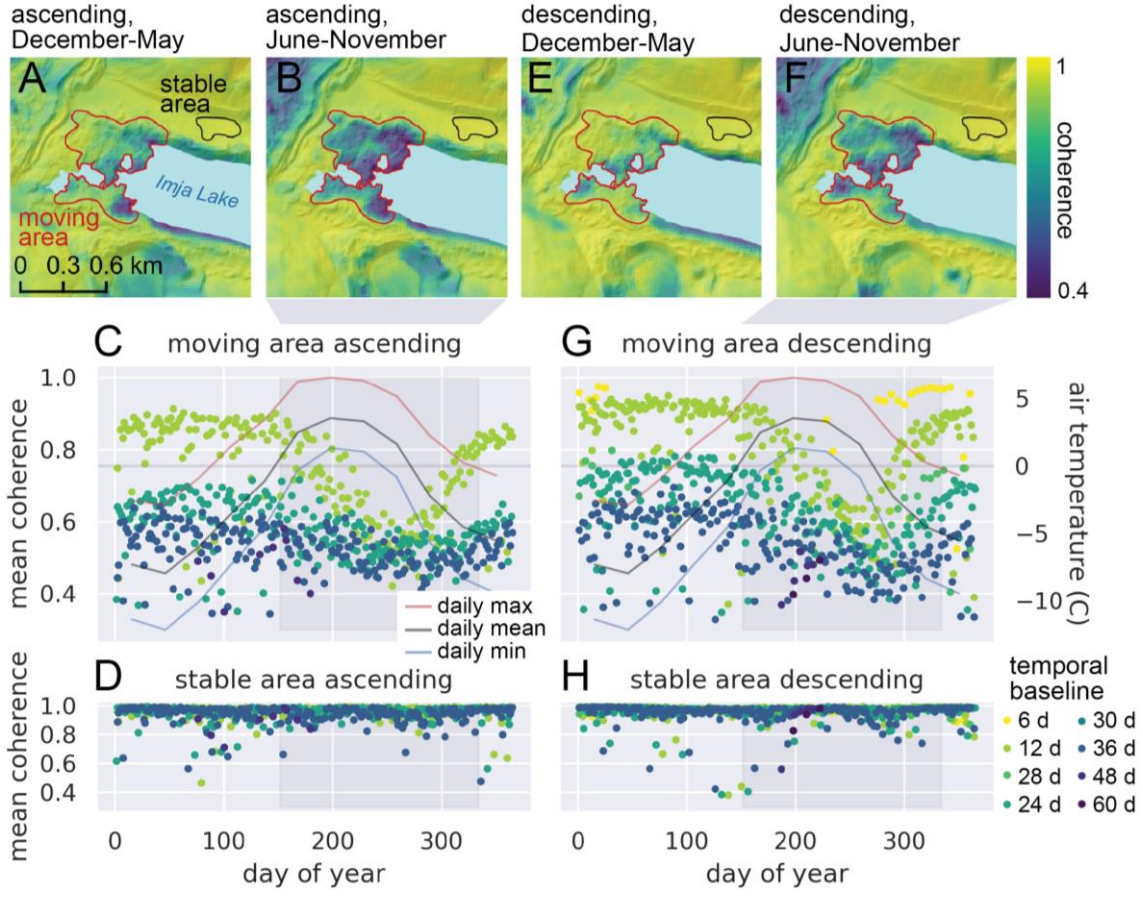

Figure 2: Imja Lake moraine dam InSAR coherence and air temperature. Mean coherence maps for all 439 12-day pairs of ascending Sentinel-1 SAR images during the colder months (A) and warmer months (B). C) Mean coherence of the moraine dam moving area in all ascending interferograms. Lines show mean daily maximum, mean, and minimum air temperature for each month from the nearby Pyramid Weather Station (UCAR/NCAR-Earth Observing Laboratory et al., 2011). D) Mean coherence of the stable area for all ascending interferograms. Panels E-H show corresponding plots for descending pairs.

The decrease in coherence is spatially constrained. Visual inspection of mean coherence maps from the annual high-coherence period (December-May) and low-coherence period (June-November) revealed that coherence decreased over almost all of the moraine dam moving area (Fig 2A, B, C, D). Several areas of low coherence in December-May expanded and displayed a further decrease in coherence during June-November. Areas of high-coherence in December-May also displayed a decrease in coherence during June-November. Low-coherence areas were mostly consistent between ascending and descending orbits, with minor discrepancies potentially explained by differences in the LOS and acquisition time (18:00 local for ascending, 07:00 local for descending) of the two relative orbits.

https://doi.org/10.5194/egusphere-2024-3196
Preprint. Discussion started: 8 November 2024

5.2 Feature-tracking offset maps

The feature-tracking offset maps showed coherent motion of the moraine dam surface. The spatial mean of the per-pixel median LOS velocity over the moving area was +13.6 cm/yr for the ascending orbit and +7.2 cm/yr for the descending orbit, with maximum per-pixel median LOS velocity of +46.1 cm/yr for the ascending orbit and +29.3 cm/yr for the descending orbit (Fig. 3A, B). For both orbits, higher velocity was observed on the eastern side of the moving area near the lake shoreline. Mean feature tracking SNR over the moraine dam moving area was 11.4 for the ascending orbit and 14.0 for the descending orbit (Fig. 3C, D). The spatial mean of the per-pixel NMAD of LOS velocity was 11.7 cm/yr for the ascending orbit and 13.1 cm/yr for the descending orbit (Fig. 3E, F). The spatial mean of per-pixel median LOS velocity over the stable area was 0.7 cm/yr for the ascending track and -0.3 cm/yr for the descending track, though feature tracking velocity was ultimately masked in these areas with high InSAR coherence prior to inversion.

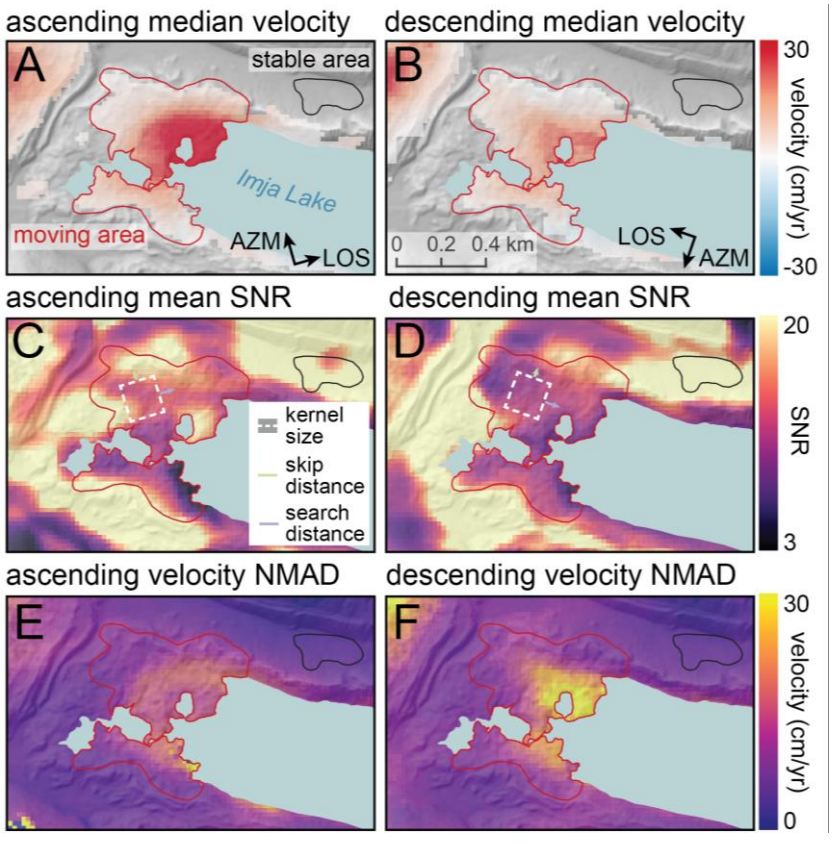

Figure 3: Sentinel-1 SAR image feature tracking results for the full 2017-2024 time series for all 192 pairs on ascending (left) and 210 pairs on descending (right) orbits. A, B) Per-pixel median feature tracking velocity in the range direction (along the line-of-sight). Results are masked in areas with high InSAR coherence, where feature tracking products are not used during inversion. C, D) Per-pixel median signal-to-noise ratio. E, F) Per-pixel normalized median absolute deviation (NMAD) of the feature tracking velocity in range direction. Higher values are observed for locations with 1) greater temporal variability, 2) fewer reliable displacement measurements, or 3) larger measurement error.

https://doi.org/10.5194/egusphere-2024-3196
Preprint. Discussion started: 8 November 2024

5.3 Cumulative displacement time series from combined InSAR and feature tracking inversion

Most pixels in the moving area showed positive range change (i.e., movement away from the satellite) over the course of the study period for both ascending and descending orbits (Fig. 4A, B). The mean total LOS displacement of the moraine dam moving area over the 7-year study period was 97.0 cm for the ascending orbit and 46.8 cm for the descending orbit, with maximum LOS displacement of 335.3 cm for the ascending orbit and 208.7 cm for the descending orbit. The largest displacements were observed on the east side of the moving area near the lake shore, while limited displacement was observed on the northern, southern, and western margins of the moving area. While many pixels displayed constant LOS velocities over time, others showed apparent seasonal fluctuations (Fig. 4E, F). The mean apparent total LOS displacement of the stable area over the study period was -0.1 cm for the ascending orbit and -1.2 cm for the descending orbit (Fig. 4E, F).

After decomposing the LOS displacement into vertical and east/west displacement, we found that the observed LOS displacement of the moraine dam is consistent with downward and eastward motion (Fig. 4B, C). The mean total vertical displacement of the moraine dam moving area over the study period was -90.5 cm, with a maximum total vertical displacement of -330.6 cm. The mean total eastward displacement was 40.7 cm, with a maximum displacement of 181.6 cm. Over the stable area, the mean total vertical and horizontal displacement was 0.6 cm and 0.8 cm, respectively. While some pixels showed constant velocity over time, the pixels with highest velocity displayed more seasonal variability, with increased velocity during the warmer months (Fig. 4G, H).

https://doi.org/10.5194/egusphere-2024-3196
Preprint. Discussion started: 8 November 2024

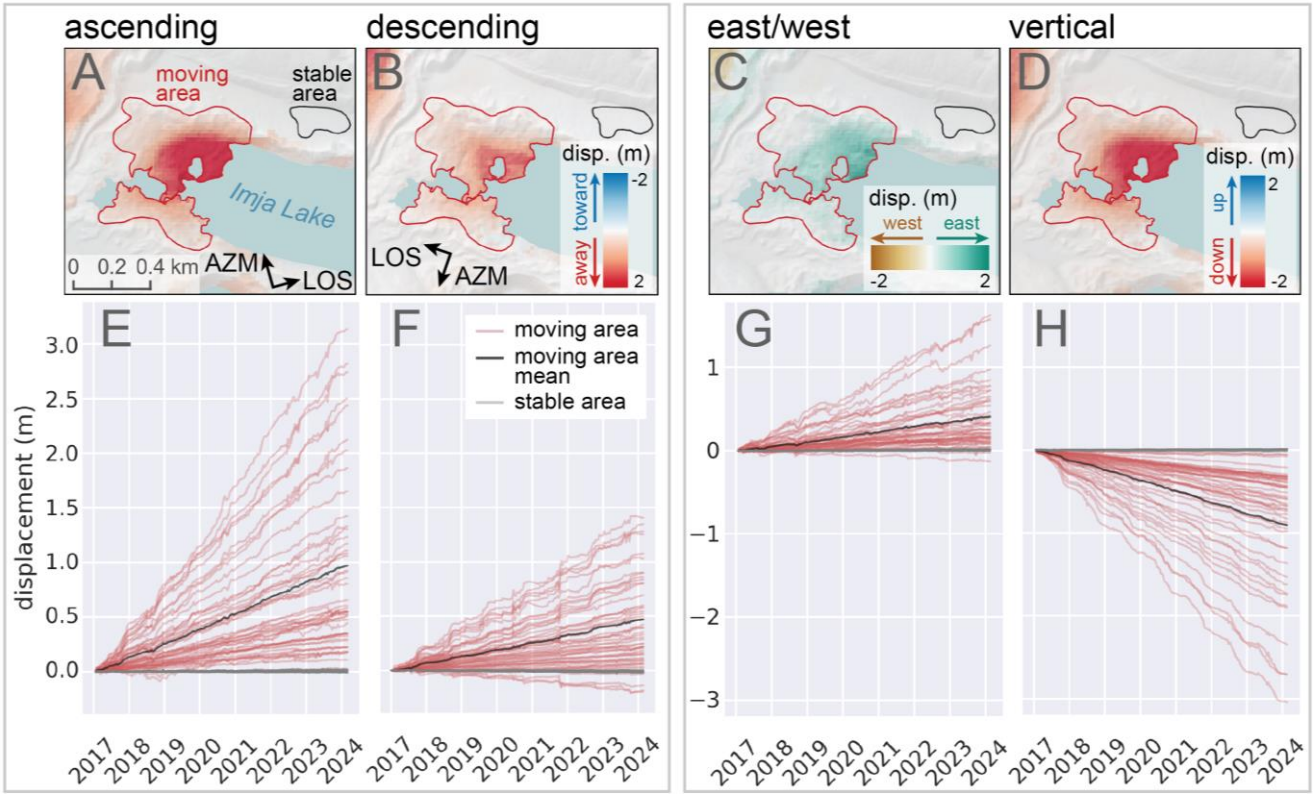

Figure 4: Cumulative displacement time series from the combined InSAR and feature tracking inversion. A, B, C, D) Maps showing total cumulative displacement of the moraine dam and stable area over the study period for the ascending (A) and descending (B) orbits, and the east/west (C) and vertical (D) directions. E, F, G, H). Cumulative displacement time series for 50 randomly-selected pixels in the moving area (red lines) and 50 randomly-selected pixels in the stable area (grey lines). The black lines show mean velocity of all pixels in the moving area.

5.4 Moraine dam velocity

The monthly median velocity maps show year-round movement of the moraine dam with a clear seasonal cycle. Vertical velocity was lowest (between -8.5 cm/yr and -9.4 cm/yr) in January, February, March, and April (Fig. 5A, B) while mean stable area vertical velocity was -0.1 to +0.6 cm/yr during the same months. The moraine dam moving area vertical velocity increased from May through October, when the mean vertical velocity reached -21.0 cm/yr (Fig. 5A, B). Vertical velocity over the moraine dam moving area then decreased in November and December (Fig. 5A).

https://doi.org/10.5194/egusphere-2024-3196
Preprint. Discussion started: 8 November 2024

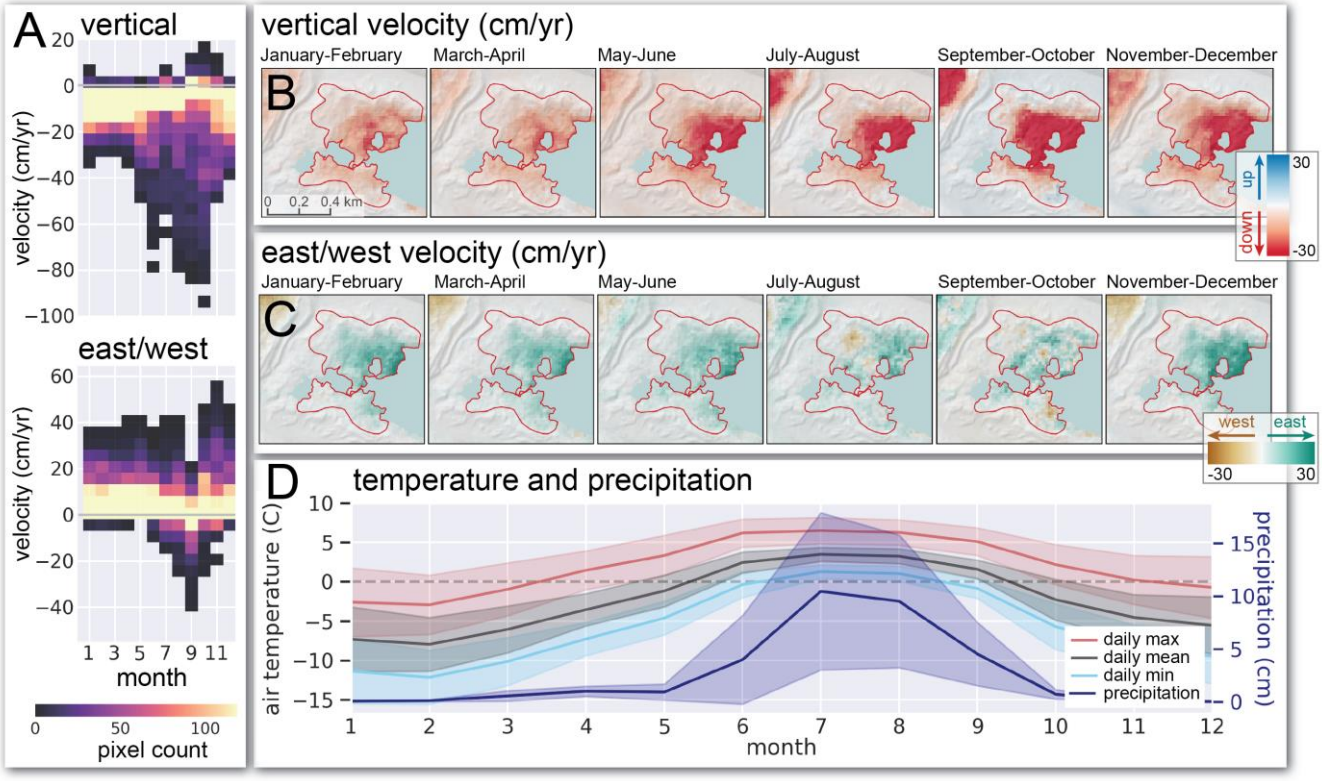

Figure 5: Monthly surface velocity of the Imja Lake moraine dam from the combined InSAR and feature tracking inversion. A) Histograms showing distribution of median monthly surface velocity values in the moving area over time. B, C) Maps showing vertical and east/west median surface velocity during bimonthly periods. D) Mean daily air temperature and precipitation for each month at the nearby Pyramid Weather Station (UCAR/NCAR-Earth Observing Laboratory et al., 2011). Shaded areas show one standard deviation.

From December-May, the mean horizontal velocity of the moraine dam moving area was 6.6 to 8.1 cm/yr to the east, with limited pixel-to-pixel variability (Fig. 5A, C). Between June and September, some pixels began to move westward, and pixel-to-pixel variability increased (Fig. 5A, C). Mean east/west velocity in the moving area decreased from June through September (Fig. 5A, C).

5.5 Evidence for buried ice

We observed a substantial decrease (0.34) in median coherence over the moraine dam moving area between the winter to early spring (0.92) and late summer (0.58) (Fig. 6A). There was no measurable decrease over the stable area.

https://doi.org/10.5194/egusphere-2024-3196
Preprint. Discussion started: 8 November 2024

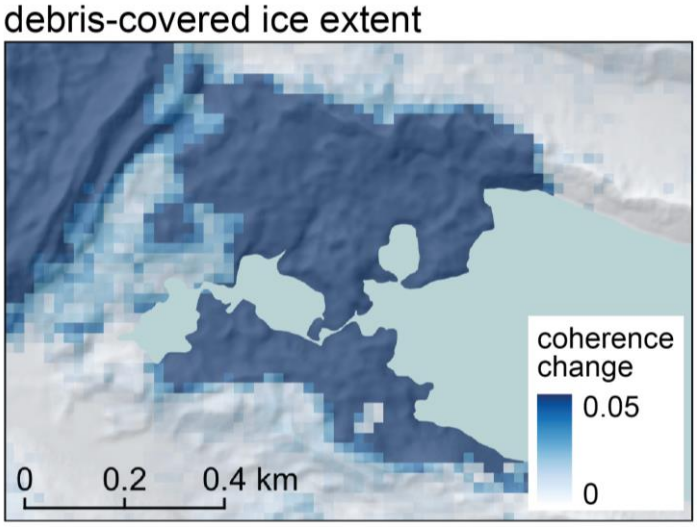

Figure 6: Seasonal change in median coherence offers a proxy to map the spatial distribution of buried ice.

6 Discussion

Our combined InSAR and feature tracking surface displacement results can be used along with coherence change results to both infer the primary processes responsible for moraine dam degradation, and to constrain the timing and magnitude of those processes.

6.1 Ice melt

We interpret the observed seasonal decrease in coherence to be caused by melting of buried ice and associated debris reworking. The lag between the onset of air temperatures above freezing and melt onset (Fig. 2) is likely related to debris cover insulation. Melt of buried ice and debris reworking changes the moraine surface morphometry, altering the scattering characteristics of the surface and decreasing coherence. Backwasting and thermokarst development should also lead to large coherence decreases.

Other processes could also contribute to decreased coherence during warmer months. Exposure of interstitial ice and snow in the upper debris layer could cause a decrease in coherence. Meltwater from massive or interstitial ice may further cause changes in surface water distribution and soil moisture, contributing to decreased coherence (e.g. Lu & Meyer, 2002; Nolan et al., 2003). Increased summer precipitation (Fig. 5D) can also affect surface water and soil moisture. Changes in surface water and soil moisture driven by summer precipitation are expected to impact the dielectric properties of the moraine dam and the nearby stable area similarly. Surface snow and interstitial ice in the upper debris layer may also be present over both the stable area and the moraine dam. However, no loss of coherence was observed over the stable area during the warmer months (Fig. 2G,

https://doi.org/10.5194/egusphere-2024-3196
Preprint. Discussion started: 8 November 2024

H), suggesting that seasonal melt of massive buried ice is primarily responsible for the observed coherence loss over the moraine dam.

The observed spatial variability in seasonal coherence change may be explained by debris thickness and proximity to the lake and surface ponds, which can enhance downwasting and backwasting (Johnson, 1971; Driscoll, 1980; Pickard, 1983; Watanabe et al., 1995). Low coherence during colder months was observed in some locations, especially bordering the lake and surface ponds (Fig. 2A, C). When air temperatures are below freezing, these locations potentially experience additional ice degradation and associated debris reworking due to melt caused by contact with water and by calving.

During the warmer months, we observed a clear increase in subsidence over much of the moraine dam (Fig. 5A, B), likely associated with melting of buried ice. The highest downward velocity was observed in October with mean moving area velocity of -21 cm/yr. Increases in velocity were first observed over the northern margin of the lake and surface ponds, suggesting earlier melt in these locations. Small areas of apparent upward displacement at the southern margin of the lake are likely caused by consistent unwrapping errors due to low coherence (Fig. 2B, D; Fig. 5B). East-west displacement during the warmer months was variable, with some areas mostly moving east and some areas mostly moving west (Fig. 5C). This variability in horizontal displacement direction could be caused by the variable topography of the moraine dam, as the direction of displacement caused by melt of sloped ice surfaces depends on the aspect of the surface.

If we extrapolate the observed 2017 to 2024 mean subsidence rates forward in time, and consider the current moraine dam topography, we find that the northeast area of the moraine dam bordering the lake edge is most vulnerable to subsidence below the current lake level. This topographic evolution would result in westward expansion of Imja Lake, decreasing the width of the moraine dam.

6.2 Ice flow

During the colder months, we observed clear and widespread downward and eastward displacement over the surface of the moraine dam with a mean velocity within the moving area of -10.5 and 7.3 cm/yr respectively (Fig. 5A, B, C). The high coherence values over the moraine dam during colder months (Fig. 2A, C, E, F) provide high confidence in these measurements. Assuming that air temperatures during this period were mostly below freezing, we do not attribute this displacement to melt of buried ice. While debris settling and frost creep could potentially explain some component of downward and horizontal motion, they are not expected to cause displacement of this magnitude on these time scales and we do not observe similar motion over debris outside the moraine dam (Colman & Pierce, 1986; Bursik, 1991; Hallet & Putkonen, 1994). We instead attribute this motion primarily to flow of the thick, massive ice within the moraine dam.

https://doi.org/10.5194/egusphere-2024-3196
Preprint. Discussion started: 8 November 2024

Downward and eastward movement is consistent with along-slope flow for the broad moraine dam slopes (Supplemental Fig. 1). The mean surface slope of the moving area is 9.5˚. Somos-Valenzuela et al. (2012) found evidence for ice bottom depths between 30 and 60 m over much of the moraine dam surface. Assuming debris thickness of less than 1-20 m (Hambrey et al., 2008), most ice deposits in the moraine dam may have thicknesses between 10 and 60 m. Higher observed surface velocity during colder months appears to correspond to areas with deeper ice bottom depths. The highest velocity was observed near the north margin of the lake, the area with the deepest mapped ice bottom depths. Near-zero velocity was observed over the southwest portion of the moraine dam, where Dahal et al., (2018) observed discontinuous blocks of buried ice.

While we suggest that ice flow can explain some observed surface displacement during colder months, we cannot rule out displacement caused by sliding along planes of weakness, which may include ice thrust planes, closed crevasses, and/or the ice-bed interface. Even in cold months, liquid water from the lake or surface ponds could be responsible for saturating moraine material at depth, increasing pore water pressure. In the summer, melt may provide additional water to planes of weakness, further decreasing pore pressure and contributing to increased velocities, as is observed with glaciers (e.g. Bartholomew et al., 2010; Iverson, 2010; Minchew & Meyer, 2020), rock glaciers (e.g. Ikeda et al., 2008; Kenner et al., 2017; Cicoira et al., 2019), and landslides (e.g. Bayer et al., 2018; Handwerger et al., 2019).

Previous surface displacement measurements also provide evidence for ice flow. Watanabe et al. (1995) described westward movement of -0.96 m/yr, consistent with the original flow direction of Imja Glacier. Fujita et al., (2009) described horizontal flow rates of less than 0.17 m/yr in an unspecified direction. Thus, our results suggest there was a reversal of the flow direction from downvalley flow to the west in the 1990s to the eastward flow toward Imja Lake during the 2017-2024 study period.

The observed change in flow direction is likely related to evolving thickness of lower Imja Glacier though differential ablation both above and below the lake surface (Kjær & Krüger, 2001), changing longitudinal stresses associated with decoupling from the active flowing glacier during retreat, and interaction with the expanding lake. Moraine dam topography and lake bathymetry suggests that buried ice within the moraine dam is likely thicker than ice under the lake to the east, resulting in a west to east ice thickness gradient (Haritashya et al., 2018). Complete decoupling from the active glacier will remove compressive longitudinal stress contributing to downvalley movement. Complex interactions between the evolving glacier and the growing lake to the east would likely also recharacterize the stress regime, as has been observed for lake-terminating glaciers in the region (King et al., 2018). Our detailed displacement time series can be used to constrain ice and debris evolution models, which are needed to better understand the Imja Lake moraine dam evolution and implications for changing structural stability.

6.3 Buried ice extent

We assume that the characteristic seasonal decrease in InSAR coherence over the moraine dam is caused by seasonal melt of buried ice. As such, where the magnitude of the seasonal change in coherence is large, we assume that internal ice is present.

https://doi.org/10.5194/egusphere-2024-3196
Preprint. Discussion started: 8 November 2024

We find evidence for buried ice over most of the moraine dam, including areas displaying near-zero surface displacement. A smaller seasonal change in coherence is observed over the southwest corner of the dam near the outlet, which is consistent with the isolated ice deposits mapped by Dahal et al., (2018). The magnitude of seasonal coherence change is likely also related to overlying debris thickness, as thicker debris 1) provides more insulation, suppressing melt and 2) experiences less surface change per quantity of melt at depth.

6.4 Limitations

While our InSAR and feature tracking results improve our understanding of the processes responsible for moraine dam degradation, it is important to discuss some limitations. For example, while feature tracking is more robust to large surface changes and deformation gradients than InSAR, surface change can result in poor image correlation and unreliable displacement measurements. Our combined inversion approach attempts to leverage the strengths of both methods, but it is still unable to capture some features and processes, like iceberg calving, backwasting, and fast-moving debris flows.

Overall, we potentially underestimate surface displacement caused by processes that result in significant and localized surface change, rather than uniform movement of the surface. This underestimation can partly explain why our maximum vertical velocity over the moraine dam surface was only -0.47 m/yr compared to -1.9 m/yr from Haritashya et al. (2018). However, we note that these two studies covered different time periods, and there are known quality issues with the Shuttle Radar Topography Mission (SRTM) DEM used by Haritashya et al. (2018). Additional measurements from very-high-resolution satellite images and DEM time series would quantify surface displacement related to calving and ice cliff retreat.

We further consider limitations related to our time-series processing approach. Combining InSAR and feature tracking produces displacement time series that are more accurate than time series produced independently. However, because feature tracking measures the displacement of groups of pixels (10 in azimuth by 60 in range, or 141 by 138 m), it provides inherently lower-resolution displacement measurements than InSAR (Joughin, 2002). By integrating both InSAR and feature tracking measurements, we effectively degrade the spatial resolution of our InSAR measurements in exchange for improved displacement accuracy during the warmer months when surface change between Sentinel-1 acquisitions results in reduced InSAR coherence.

We finally acknowledge limitations of the Sentinel-1 acquisition geometry, with only ~10% of any real north-south displacement mapped into line-of-sight measurements for this location. We combined data from ascending and descending passes to calculate east/west and vertical displacement, assuming that north/south displacement does not substantially contribute to the displacement observations. In fact, some small contribution from north/south displacement is expected, which potentially introduces a source of error in our measurements of surface velocity (Brouwer & Hanssen, 2021). If we assume that true north/south displacement is equal to true east/west displacement, this will cause a 0.5% error in our calculated east

https://doi.org/10.5194/egusphere-2024-3196
Preprint. Discussion started: 8 November 2024

displacement and a 6.3% error in our calculated up/down displacement. Given the observed surface geometry of the Imja Lake moraine dam and the valley, we expect primarily east/west motion.

7 Conclusions

We demonstrated that Sentinel-1 InSAR and feature tracking can be used to measure displacement of an ice-cored moraine dam bounding Imja Lake in Nepal. By combining InSAR and feature tracking measurements, we created a surface displacement time series that is more accurate than using InSAR or feature tracking alone. We find that a 0.3 km^2 area of the moraine dam subsided an average of ~90 cm over the 7-year study period, and the northeast area of the moraine dam bordering the lake edge is most vulnerable to subsidence below the current lake level.

We observed a systematic seasonal cycle in InSAR coherence values over the moraine dam surface, with a substantial decrease in coherence occurring about 60 days after mean daily maximum air temperatures rise above 0°C. We show that seasonal changes in InSAR coherence can be used to map buried ice within the moraine dam, with an observed spatial distribution that is consistent with previous geophysical surveys.

We find evidence that the primary processes contributing to moraine dam degradation are buried ice melt and ice flow. Buried ice melt occurs in the summer and fall, resulting in a seasonal increase in downward vertical velocity (from about -9 to -21 cm/yr on average) and variable horizontal velocity over the surface of the moraine dam. Ice flow occurs year-round and results mostly in downward and eastward movement. Our surface velocity measurements, alongside historical measurements, provide evidence that the Imja Lake moraine dam is undergoing kinematic changes which we attribute to changing ice thicknesses, decoupling from the Imja Glacier, and interaction with Imja Lake.

Collectively, our findings demonstrate the potential for SAR remote sensing to quantify the evolution of moraine dam degradation and provide new information about moraine dam internal structure. This information may be valuable when assessing GLOF hazards, performing in-situ investigations, and planning hazard remediation activities. In the future, we hope to extend our analysis to other high-priority moraine dams in the region and to integrate additional techniques for remote measurement of surface change.

Code availability

All source code and documentation is available on Github. The fufiters repository (https://github.com/relativeorbit/fufiters) contains code and documentation for reproducible data processing, and the fufiters_imja_analysis (https://github.com/gbrencher/fufiters_imja_analysis) repository contains code for data analysis and figure preparation.

https://doi.org/10.5194/egusphere-2024-3196
Preprint. Discussion started: 8 November 2024

Data Availability

All Sentinel-1 data are freely available from the Alaska Satellite Facility (ASF) Distributed Active Archive Center (DAAC).

Author Contribution

GB conceptualized this work with input from DS. GB and SH designed the methodology and built the software. GB performed the analysis and prepared the manuscript with substantial input from DS and SH.

Competing Interests

The authors declare that they have no conflict of interest.

Acknowledgements

GB was supported by NSF GRFP DGe-2140004. Analysis was performed using CryoCloud (NASA grants 80NSSC22K1877, 80NSSC23K0002). DS was supported by NASA awards 80NSSC20K1595 and 80NSSC24K1633. SH was supported by NSF award 2117834 and NASA award 80NSSC22K0345.

References

Ali Badal, L. (2023, October 6). Indian soldier's body found in Teesta handed over to BSF. Dhaka Tribune. https://www.dhakatribune.com/bangladesh/nation/327225/indian-soldier%E2%80%99s-body-found-in-teesta-handed-over

Allen, S.K., Linsbauer, A., Randhawa, S.S., Huggel, C., Rana, P., & Kumari, A. (2016). Glacial lake outburst flood risk in Himachal Pradesh, India: An integrative and anticipatory approach considering current and future threats. Natural Hazards, 84(3), 1741–1763. https://doi.org/10.1007/s11069-016-2511-x

Bartholomew, I., Nienow, P., Mair, D., Hubbard, A., King, M. A., & Sole, A. (2010). Seasonal evolution of subglacial drainage and acceleration in a Greenland outlet glacier. Nature Geoscience, 3(6), 408–411. https://doi.org/10.1038/ngeo863

Bayer, B., Simoni, A., Mulas, M., Corsini, A., & Schmidt, D. (2018). Deformation responses of slow moving landslides to seasonal rainfall in the Northern Apennines, measured by InSAR. Geomorphology, 308, 293–306. https://doi.org/10.1016/j.geomorph.2018.02.020

Bertone, A., Barboux, C., Bodin, X., Bolch, T., Brardinoni, F., Caduff, R., Christiansen, H. H., Darrow, M. M., Delaloye, R., Etzelmüller, B., Humlum, O., Lambiel, C., Lilleøren, K. S., Mair, V., Pellegrinon, G., Rouyet, L., Ruiz, L., & Strozzi,

https://doi.org/10.5194/egusphere-2024-3196
Preprint. Discussion started: 8 November 2024

T. (2022). Incorporating InSAR kinematics into rock glacier inventories: Insights from 11 regions worldwide. The Cryosphere, 16(7), 2769–2792. https://doi.org/10.5194/tc-16-2769-2022

Brouwer, W. S., & Hanssen, R. F. (2021). An Analysis of Insar Displacement Vector Decomposition Fallacies and the Strap-Down Solution. 2021 IEEE International Geoscience and Remote Sensing Symposium IGARSS, 2927–2930. https://doi.org/10.1109/IGARSS47720.2021.9554216

Budhathoki, K. P., Bajracharya, O., & Pokharel, B. (1970). Assessment of Imja Glacier Lake outburst Flood (GLOF) Risk in Dudh Koshi River Basin using Remote Sensing Techniques. Journal of Hydrology and Meteorology, 7(1), 75–91. https://doi.org/10.3126/jhm.v7i1.5618

Bürgmann, R., Rosen, P. A., & Fielding, E. J. (2000). Synthetic Aperture Radar Interferometry to Measure Earth's Surface Topography and Its Deformation. Annual Review of Earth and Planetary Sciences, 28(1), 169–209. https://doi.org/10.1146/annurev.earth.28.1.169

Bursik, M. (1991). Relative Dating of Moraines Based on Landform Degradation, Lee Vining Canyon, California. Quaternary Research, 35(3-Part1), 451–455. https://doi.org/10.1016/0033-5894(91)90057-C

Cabré, A., Remy, D., Aguilar, G., Carretier, S., & Riquelme, R. (2020). Mapping rainstorm erosion associated with an individual storm from InSAR coherence loss validated by field evidence for the Atacama Desert. Earth Surface Processes and Landforms, 45(9), 2091–2106. https://doi.org/10.1002/esp.4868

Carrivick, J. L., & Tweed, F. S. (2016). A global assessment of the societal impacts of glacier outburst floods. Global and Planetary Change, 144, 1–16. https://doi.org/10.1016/j.gloplacha.2016.07.001

Chini, M., Pelich, R., Pulvirenti, L., Pierdicca, N., Hostache, R., & Matgen, P. (2019). Sentinel-1 InSAR Coherence to Detect Floodwater in Urban Areas: Houston and Hurricane Harvey as A Test Case. Remote Sensing, 11(2), Article 2. https://doi.org/10.3390/rs11020107

Choudhury, S.N., & Hussain, Z. (2023, October 5). Floods in India's Sikkim state leave 10 dead, 82 missing. Reuters. https://www.reuters.com/world/india/nearly-two-dozen-indian-troops-missing-after-flash-flood-ani-2023-10-04/

Cicoira, A., Beutel, J., Faillettaz, J., & Vieli, A. (2019). Water controls the seasonal rhythm of rock glacier flow. Earth and Planetary Science Letters, 528, 115844. https://doi.org/10.1016/j.epsl.2019.115844

Colman, S. M., & Pierce, K. L. (1986). Glacial Sequence Near McCall, Idaho: Weathering Rinds, Soil Development, Morphology, and Other Relative-Age Criteria. Quaternary Research, 25(1), 25–42. https://doi.org/10.1016/0033-5894(86)90041-4

Costa, J. E., & Schuster, R. L. (1988). The formation and failure of natural dams. GSA Bulletin, 100(7), 1054–1068. https://doi.org/10.1130/0016-7606(1988)100<1054:TFAFON>2.3.CO;2

Dahal, P., Paudyal, K., & Rajaure, S. (2018). Geophysical study on moraine dam of Imja Glacial Lake in Eastern Nepal using Electrical Resistivity Tomography Method. Journal of Nepal Geological Society, 55, 15–22. https://doi.org/10.3126/jngs.v55i1.22784

https://doi.org/10.5194/egusphere-2024-3196
Preprint. Discussion started: 8 November 2024

Emmer, A., & Cochachin, A. (2013). The causes and mechanisms of moraine-dammed lake failures in the Cordillera Blanca, North American Cordillera, and Himalayas. AUC GEOGRAPHICA, 48(2), 5–15. https://doi.org/10.14712/23361980.2014.23

Emmer, A., Vilímek, V., & Zapata, M. l. (2018). Hazard mitigation of glacial lake outburst floods in the Cordillera Blanca (Peru): The effectiveness of remedial works. Journal of Flood Risk Management, 11(S1), S489–S501. https://doi.org/10.1111/jfr3.12241

European Space Agency. (2021). Copernicus Digital Elevation Model (DEM) [Computer software]. https://registry.opendata.aws/copernicus-dem/

European Space Agency. (2022). Copernicus DEM Product Handbook (v4.0) [Computer software]. https://spacedata.copernicus.eu/documents/20123/121239/GEO1988-CopernicusDEM-SPE-002_ProductHandbook_I4.0.pdf/92df0801-6714-20e4-75ae-0be634b9e301?t=1666775307957

Fahnestock, M., Bindschadler, R., Kwok, R., & Jezek, K. (1993). Greenland Ice Sheet Surface Properties and Ice Dynamics from ERS-1 SAR Imagery. Science, 262(5139), 1530–1534. https://doi.org/10.1126/science.262.5139.1530

Fahnestock, M., Scambos, T., Moon, T., Gardner, A., Haran, T., & Klinger, M. (2016). Rapid large-area mapping of ice flow using Landsat 8. Remote Sensing of Environment, 185, 84–94. https://doi.org/10.1016/j.rse.2015.11.023

Fuhrmann, T., & Garthwaite, M. C. (2019). Resolving Three-Dimensional Surface Motion with InSAR: Constraints from Multi-Geometry Data Fusion. Remote Sensing, 11(3), Article 3. https://doi.org/10.3390/rs11030241

Fujita, K., Sakai, A., Nuimura, T., Yamaguchi, S., & Sharma, R. R. (2009). Recent changes in Imja Glacial Lake and its damming moraine in the Nepal Himalaya revealed by in situ surveys and multi-temporal ASTER imagery. Environmental Research Letters, 4(4), 045205. https://doi.org/10.1088/1748-9326/4/4/045205

Fujita, K., Sakai, A., Takenaka, S., Nuimura, T., Surazakov, A. B., Sawagaki, T., & Yamanokuchi, T. (2013). Potential flood volume of Himalayan glacial lakes. Natural Hazards and Earth System Sciences, 13(7), 1827–1839. https://doi.org/10.5194/nhess-13-1827-2013

Hallet, B., & Putkonen, J. (1994). Surface Dating of Dynamic Landforms: Young Boulders on Aging Moraines. Science, 265(5174), 937–940. https://doi.org/10.1126/science.265.5174.937

Hambrey, M. J., Quincey, D. J., Glasser, N. F., Reynolds, J. M., Richardson, S. J., & Clemmens, S. (2008). Sedimentological, geomorphological and dynamic context of debris-mantled glaciers, Mount Everest (Sagarmatha) region, Nepal. Quaternary Science Reviews, 27(25), 2361–2389. https://doi.org/10.1016/j.quascirev.2008.08.010

Handwerger, A. L., Fielding, E. J., Huang, M.H., Bennett, G. L., Liang, C., & Schulz, W. H. (2019). Widespread Initiation, Reactivation, and Acceleration of Landslides in the Northern California Coast Ranges due to Extreme Rainfall. Journal of Geophysical Research: Earth Surface, 124(7), 1782–1797. https://doi.org/10.1029/2019JF005035

Handwerger, A. L., Roering, J. J., Schmidt, D. A., & Rempel, A. W. (2015). Kinematics of earthflows in the Northern California Coast Ranges using satellite interferometry. Geomorphology, 246, 321–333. https://doi.org/10.1016/j.geomorph.2015.06.003

https://doi.org/10.5194/egusphere-2024-3196
Preprint. Discussion started: 8 November 2024

Hanisch, J., Ambarish, P., Grabs, W., Dixit, A., & Reynolds, J. (2000). GLOF mitigation strategies—Lessons learned from studying the Thulagi Glacier Lake, Nepal. Journal of Nepal Geological Society, 22. https://doi.org/10.3126/jngs.v22i0.32375

Healy, T. R. (1975). Thermokarst—A mechanism of de-icing ice-cored moraines. Boreas, 4(1), 19–23. https://doi.org/10.1111/j.1502-3885.1975.tb00676.x

Hock, R., Bliss, A., Marzeion, B., Giesen, R. H., Hirabayashi, Y., Huss, M., Radić, V., & Slangen, A. B. A. (2019). GlacierMIP – A model intercomparison of global-scale glacier mass-balance models and projections. Journal of Glaciology, 65(251), 453–467. https://doi.org/10.1017/jog.2019.22

Huggel, C., Cochachin, A., Drenkhan, F., Fluixá-Sanmartín, J., Frey, H., García Hernández, J., Jurt, C., Muñoz, R., Price, K., & Vicuña, L. (2020). Glacier Lake 513, Peru: Lessons for early warning service development. https://doi.org/10.5167/UZH-186748

Huggel, C., Salzmann, N., Allen, S., Caplan-Auerbach, J., Fischer, L., Haeberli, W., Larsen, C., Schneider, D., & Wessels, R. (2010). Recent and future warm extreme events and high-mountain slope stability. Philosophical Transactions of the Royal Society A: Mathematical, Physical and Engineering Sciences, 368(1919), 2435–2459. https://doi.org/10.1098/rsta.2010.0078

Ikeda, A., Matsuoka, N., & Kääb, A. (2008). Fast deformation of perennially frozen debris in a warm rock glacier in the Swiss Alps: An effect of liquid water. Journal of Geophysical Research: Earth Surface, 113(F1). https://doi.org/10.1029/2007JF000859

Irvine-Fynn, T. D. L., Barrand, N. E., Porter, P. R., Hodson, A. J., & Murray, T. (2011). Recent High-Arctic glacial sediment redistribution: A process perspective using airborne lidar. Geomorphology, 125(1), 27–39. https://doi.org/10.1016/j.geomorph.2010.08.012

Itoh, K. (1982). Analysis of the phase unwrapping algorithm. Applied Optics, 21(14), 2470–2470. https://doi.org/10.1364/AO.21.002470

Iverson, N. R. (2010). Shear resistance and continuity of subglacial till: Hydrology rules. Journal of Glaciology, 56(200), 1104–1114. https://doi.org/10.3189/002214311796406220

Jiang, L., Fan, X., Deng, Y., Zou, C., Feng, Z., Djukem, D. L. W., ... & Xu, Q. (2023). Combining geophysics, remote sensing and numerical simulation to assess GLOFs: Case study of the Namulacuo Lake in the Southeastern Tibetan Plateau. Science of The Total Environment, 880, 163262.

Johnson, P. G. (1971). Ice Cored Moraine Formation and Degradation, Donjek Glacier, Yukon Territory, Canada. Geografiska Annaler: Series A, Physical Geography, 53(3–4), 198–202. https://doi.org/10.1080/04353676.1971.11879845

Joughin, I. (2002). Ice-sheet velocity mapping: A combined interferometric and speckle-tracking approach. Annals of Glaciology, 34, 195–201. https://doi.org/10.3189/172756402781817978

Joughin, I., Smith, B. E., & Howat, I. M. (2018). A complete map of Greenland ice velocity derived from satellite data collected over 20 years. Journal of Glaciology, 64(243), 1–11. https://doi.org/10.1017/jog.2017.73

https://doi.org/10.5194/egusphere-2024-3196
Preprint. Discussion started: 8 November 2024

Kellerer-pirklbauer, A., Lieb, G. K., Avian, M., & Carrivick, J. (2012). Climate change and rock fall events in high mountain areas: Numerous and extensive rock falls in 2007 at mittlerer burgstall, central austria. Geografiska Annaler: Series A, Physical Geography, 94(1), 59–78. https://doi.org/10.1111/j.1468-0459.2011.00449.x

Kenner, R., Phillips, M., Beutel, J., Hiller, M., Limpach, P., Pointner, E., & Volken, M. (2017). Factors Controlling Velocity Variations at Short-Term, Seasonal and Multiyear Time Scales, Ritigraben Rock Glacier, Western Swiss Alps. Permafrost and Periglacial Processes, 28(4), 675–684. https://doi.org/10.1002/ppp.1953

Khadra, N. S. (2016, October 31). Nepal drains dangerous Everest lake. BBC News. https://www.bbc.com/news/world-asia-37797559

King, O., Dehecq, A., Quincey, D., & Carrivick, J. (2018). Contrasting geometric and dynamic evolution of lake and land-terminating glaciers in the central Himalaya. Global and Planetary Change, 167, 46-60.

Kjær, K.H., & Krüger, J. (2001). The final phase of dead-ice moraine development: Processes and sediment architecture, Kötlujökull, Iceland. Sedimentology, 48(5), 935–952. https://doi.org/10.1046/j.1365-3091.2001.00402.x

Krüger, J., & Kjær, K.H. (2000). De-icing progression of ice-cored moraines in a humid, subpolar climate, Kötlujökull, Iceland. The Holocene, 10(6), 737–747.

Kumar, H., & Travelli, A. (2023, October 6). A Calamitous Flood Shows the Dangers Lurking in Melting Glaciers. The New York Times. https://www.nytimes.com/2023/10/06/world/asia/india-flood-sikkim-climate-change.html

Lippl, S., Vijay, S., & Braun, M. (2018). Automatic delineation of debris-covered glaciers using InSAR coherence derived from X-, C- and L-band radar data: A case study of Yazgyl Glacier. Journal of Glaciology, 64(247), 811–821. https://doi.org/10.1017/jog.2018.70

Liu, H., Zhao, Z., & Jezek, K. C. (2007). Synergistic Fusion of Interferometric and Speckle-Tracking Methods for Deriving Surface Velocity From Interferometric SAR Data. IEEE Geoscience and Remote Sensing Letters, 4(1), 102–106. https://doi.org/10.1109/LGRS.2006.885885

Lu, Z., & Meyer, D. J. (2002). Study of high SAR backscattering caused by an increase of soil moisture over a sparsely vegetated area: Implications for characteristics of backscattering. International Journal of Remote Sensing, 23(6), 1063–1074. https://doi.org/10.1080/01431160110040035

Lukas, S., Nicholson, L. I., Ross, F. H., & Humlum, O. (2005). Formation, meltout processes and landscape alteration of high-Arctic ice-cored moraines—Examples from Nordenskiold Land, central Spitsbergen. Polar Geography, 29(3), 157-187.

Lukas, S. (2011). Ice-cored moraines, Encyclopedia of Snow, Ice and Glaciers. Springer.

Massonnet, D., & Feigl, K. L. (1998). Radar interferometry and its application to changes in the Earth's surface. Reviews of Geophysics, 36(4), 441–500. https://doi.org/10.1029/97RG03139

Minchew, B. M., & Meyer, C. R. (2020). Dilation of subglacial sediment governs incipient surge motion in glaciers with deformable beds. Proceedings of the Royal Society A: Mathematical, Physical and Engineering Sciences, 476(2238), 20200033. https://doi.org/10.1098/rspa.2020.0033

https://doi.org/10.5194/egusphere-2024-3196
Preprint. Discussion started: 8 November 2024

Mool, P. K., Maskey, P. R., Koirala, A., Joshi, S. P., Lizong, W., Shrestha, A. B., Eriksson, M., Gurung, B., Pokharel, B., Khanal, N. R., Panthi, S., Adhikari, T., Kayastha, R. B., Ghimire, P., Thapa, R., Shrestha, B., Shrestha, S., & Shrestha, R.B. (2011). Glacial lakes and glacial lake outburst floods in Nepal. https://policycommons.net/artifacts/1516291/glacial-lakes-and-glacial-lake-outburst-floods-in-nepal/2192662/

Neupane, R., Chen, H., & Cao, C. (2019). Review of moraine dam failure mechanism. Geomatics, Natural Hazards and Risk, 10(1), 1948–1966. https://doi.org/10.1080/19475705.2019.1652210

Nie, Y., Liu, Q., Wang, J., Zhang, Y., Sheng, Y., & Liu, S. (2018). An inventory of historical glacial lake outburst floods in the Himalayas based on remote sensing observations and geomorphological analysis. Geomorphology, 308, 91–106. https://doi.org/10.1016/j.geomorph.2018.02.002

Nolan, M., Fatland, D. R., & Hinzman, L. (2003). DInSAR measurement of soil moisture. IEEE Transactions on Geoscience and Remote Sensing, 41(12), 2802–2813. https://doi.org/10.1109/TGRS.2003.817211

NSDDA. (1998). Geospatial positioning accuracy standards part 3: National standard for spatial data accuracy (no. FGDC-STD-007.3-1998).

Ohki, M., Abe, T., Tadono, T., & Shimada, M. (2020). Landslide detection in mountainous forest areas using polarimetry and interferometric coherence. Earth, Planets and Space, 72(1), 67. https://doi.org/10.1186/s40623-020-01191-5

Østrem, G. (1959). Ice Melting under a Thin Layer of Moraine, and the Existence of Ice Cores in Moraine Ridges. Geografiska Annaler. https://www.tandfonline.com/doi/abs/10.1080/20014422.1959.11907953

Porter, C., Howat, I., Husby, E., Noh, M.J., Khuvis, S., Danish, E., Tomko, K., Gardiner, J., Negrete, A., Yadav, B., Klassen, J., Kelleher, C., Cloutier, M., Bakker, J., Enos, J., Arnold, G., Bauer, G., Morin, P. (2022). EarthDEM – Strips, Version 1. Harvard Dataverse, V1. https://doi.org/10.7910/DVN/LHE9O7

Rana, B., Shrestha, A. B., Reynolds, J. M., & Aryal, R. (2000). Hazard assessment of the Tsho Rolpa Glacier Lake and ongoing. Journal of Nepal Geological Society, 22, 563–570.

Ravanel, L., Duvillard, P.-A., Jaboyedoff, M., & Lambiel, C. (2018). Recent evolution of an ice-cored moraine at the Gentianes Pass, Valais Alps, Switzerland. Land Degradation & Development, 29(10), 3693–3708. https://doi.org/10.1002/ldr.3088

Riaz, S., Ali, A., & Baig, M. N. (2014). Increasing risk of glacial lake outburst floods as a consequence of climate change in the Himalayan region. https://repository.nwu.ac.za/handle/10394/13920

Richardson, S. D., & Reynolds, J. M. (2000a). An overview of glacial hazards in the Himalayas. Quaternary International, 65–66, 31–47. https://doi.org/10.1016/S1040-6182(99)00035-X

Richardson, S. D., & Reynolds, J. M. (2000b). Degradation of ice-cored moraine dams: Implications for hazard development. IAHS Publication, 264.

Rosen, P. A., Gurrola, E., Sacco, G. F., & Zebker, H. (2012). The InSAR scientific computing environment. EUSAR 2012; 9th European Conference on Synthetic Aperture Radar, 730–733. https://ieeexplore.ieee.org/abstract/document/6217174

https://doi.org/10.5194/egusphere-2024-3196
Preprint. Discussion started: 8 November 2024

Rosen, P. A., Hensley, S., Joughin, I. R., Li, F. K., Madsen, S. N., Rodriguez, E., & Goldstein, R. M. (2000). Synthetic aperture radar interferometry. Proceedings of the IEEE, 88(3), 333–382. https://doi.org/10.1109/5.838084

Rounce, D. R., Hock, R., & Shean, D. E. (2020). Glacier mass change in High Mountain Asia through 2100 using the open-source python glacier evolution model (PyGEM). Frontiers in Earth Science, 7, 331.

Rounce, D. R., McKinney, D. C., Lala, J. M., Byers, A. C., & Watson, C. S. (2016). A new remote hazard and risk assessment framework for glacial lakes in the Nepal Himalaya. Hydrology and Earth System Sciences, 20(9), 3455–3475. https://doi.org/10.5194/hess-20-3455-2016

Rounce, D. R., Watson, C. S., & McKinney, D. C. (2017). Identification of Hazard and Risk for Glacial Lakes in the Nepal Himalaya Using Satellite Imagery from 2000–2015. Remote Sensing, 9(7), Article 7. https://doi.org/10.3390/rs9070654

Sánchez-Gámez, P., & Navarro, F. J. (2017). Glacier Surface Velocity Retrieval Using D-InSAR and Offset Tracking Techniques Applied to Ascending and Descending Passes of Sentinel-1 Data for Southern Ellesmere Ice Caps, Canadian Arctic. Remote Sensing, 9(5), Article 5. https://doi.org/10.3390/rs9050442

Sattar, A., Goswami, A., Kulkarni, Anil. V., Emmer, A., Haritashya, U. K., Allen, S., Frey, H., & Huggel, C. (2021). Future Glacial Lake Outburst Flood (GLOF) hazard of the South Lhonak Lake, Sikkim Himalaya. Geomorphology, 388, 107783. https://doi.org/10.1016/j.geomorph.2021.107783

Scapozza, C., Ambrosi, C., Cannata, M., & Strozzi, T. (2019). Glacial lake outburst flood hazard assessment by satellite Earth observation in the Himalayas (Chomolhari area, Bhutan). Geographica Helvetica, 74(1), 125-139.

Schmidt, D. A., & Bürgmann, R. (2003). Time-dependent land uplift and subsidence in the Santa Clara valley, California, from a large interferometric synthetic aperture radar data set. Journal of Geophysical Research: Solid Earth, 108(B9). https://doi.org/10.1029/2002JB002267

Schomacker, A. (2008). What controls dead-ice melting under different climate conditions? A discussion. Earth-Science Reviews, 90(3), 103–113. https://doi.org/10.1016/j.earscirev.2008.08.003

Schomacker, A., & Kjær, K. H. (2008). Quantification of dead-ice melting in ice-cored moraines at the high-Arctic glacier Holmströmbreen, Svalbard. Boreas, 37(2), 211–225. https://doi.org/10.1111/j.1502-3885.2007.00014.x

Sebastian, M. (2023, October 5). Sikkim: Race against time to save 102 missing in India floods. https://www.bbc.com/news/business-66997995

Shugar, D. H., Burr, A., Haritashya, U. K., Kargel, J. S., Watson, C. S., Kennedy, M. C., Bevington, A. R., Betts, R. A., Harrison, S., & Strattman, K. (2020). Rapid worldwide growth of glacial lakes since 1990. Nature Climate Change, 10(10), Article 10. https://doi.org/10.1038/s41558-020-0855-4

Shugar, D. H., & Clague, J. J. (2011). The sedimentology and geomorphology of rock avalanche deposits on glaciers. Sedimentology, 58(7), 1762–1783. https://doi.org/10.1111/j.1365-3091.2011.01238.x

https://doi.org/10.5194/egusphere-2024-3196
Preprint. Discussion started: 8 November 2024

Somos-Valenzuela, M. A., McKinney, D. C., Byers, A. C., Rounce, D. R., & Portocarrero, C. (2013). Modeling Mitigation Strategies for Risk Reduction at Imja Lake, Nepal. Center for Research in Water Resources, University of Texas at Austin. http://hdl.handle.net/2152/27736

Somos-Valenzuela, M., McKinney, D. C., Byers, A. C., Voss, K., Moss, J., & McKinney, J. C. (2012). Ground penetrating radar survey for risk reduction at Imja Lake, Nepal. Center for Research in Water Resources, University of Texas at Austin. http://hdl.handle.net/2152/19751

Strozzi, T., Kouraev, A., Wiesmann, A., Wegmüller, U., Sharov, A., & Werner, C. (2008). Estimation of Arctic glacier motion with satellite L-band SAR data. Remote Sensing of Environment, 112(3), 636–645. https://doi.org/10.1016/j.rse.2007.06.007

Strozzi, T., Luckman, A., Murray, T., Wegmuller, U., & Werner, C. L. (2002). Glacier motion estimation using SAR offset-tracking procedures. IEEE Transactions on Geoscience and Remote Sensing, 40(11), 2384–2391. https://doi.org/10.1109/TGRS.2002.805079

Sun, S., Che, T., Wang, J., Li, H., Hao, X., Wang, Z., & Wang, J. (2015). Estimation and Analysis of Snow Water Equivalents Based on C-Band SAR Data and Field Measurements. Arctic, Antarctic, and Alpine Research, 47(2), 313–326. https://doi.org/10.1657/AAAR00C-13-135

UCAR/NCAR-Earth Observing Laboratory, Vuillermoz, E., Tartari, G., Bertolani, L., & Ueno, K. (2011). CEOP_AP: Himalayas Surface Meteorology and Radiation Data Set. Version 1.0 (1.0, p. 6 data files, 36 ancillary/documentation files, 189 MiB) [NetCDF: Network Common Data Form for CEOP (application/x-netcdf),CEOP/EOP-3 Surface Meteorology and Radiation (ASCII)]. [object Object]. https://doi.org/10.26023/ZZHE-8SAB-040R

UNDP. (2012). Community Based Flood and Glacial Lake Outburst Risk Reduction Project [Project Document]. https://www.undp.org/sites/g/files/zskgke326/files/migration/np/aa21b4ccde4230b2b26dda751438572149d185892d482a1cf417b3a1737ce05a.pdf

Wang, W., Gao, Y., Iribarren Anacona, P., Lei, Y., Xiang, Y., Zhang, G., Li, S., & Lu, A. (2018). Integrated hazard assessment of Cirenmaco glacial lake in Zhangzangbo valley, Central Himalayas. Geomorphology, 306, 292–305. https://doi.org/10.1016/j.geomorph.2015.08.013

Wang, X., Liu, S., Ding, Y., Guo, W., Jiang, Z., Lin, J., & Han, Y. (2012). An approach for estimating the breach probabilities of moraine-dammed lakes in the Chinese Himalayas using remote-sensing data. Natural Hazards and Earth System Sciences, 12(10), 3109–3122. https://doi.org/10.5194/nhess-12-3109-2012

Watanabe, T., Kameyama, S., & Sato, T. (1995). Imja Glacier Dead-Ice Melt Rates and Changes in a Supra-Glacial Lake, 1989-1994, Khumbu Himal, Nepal: Danger of Lake Drainage. Mountain Research and Development, 15(4), 293–300. https://doi.org/10.2307/3673805

Watanabe, T., Lamsal, D., & Ives, J. D. (2009). Evaluating the growth characteristics of a glacial lake and its degree of danger of outburst flooding: Imja Glacier, Khumbu Himal, Nepal. Norsk Geografisk Tidsskrift - Norwegian Journal of Geography, 63(4), 255–267. https://doi.org/10.1080/00291950903368367

https://doi.org/10.5194/egusphere-2024-3196
Preprint. Discussion started: 8 November 2024

Wright, T. J., Parsons, B. E., & Lu, Z. (2004). Toward mapping surface deformation in three dimensions using InSAR. Geophysical Research Letters, 31(1). https://doi.org/10.1029/2003GL018827

Yang, L., Lu, Z., Zhao, C., Kim, J., Yang, C., Wang, B., ... & Wang, Z. (2022). Analyzing the triggering factors of glacial lake outburst floods with SAR and optical images: a case study in Jinweng Co, Tibet, China. Landslides, 19(4), 855-864.

Yang, L., Lu, Z., Ouyang, C., Zhao, C., Hu, X., & Zhang, Q. (2023). Glacial Lake Outburst Flood Monitoring and Modeling through Integrating Multiple Remote Sensing Methods and HEC-RAS. Remote Sensing, 15(22), 5327.

Yu, Y., Li, B., Li, Y., & Jiang, W. (2024). Retrospective Analysis of Glacial Lake Outburst Flood (GLOF) Using AI Earth InSAR and Optical Images: A Case Study of South Lhonak Lake, Sikkim. Remote Sensing, 16(13), 2307.

Yunjun, Z., Fattahi, H., & Amelung, F. (2019). Small baseline InSAR time series analysis: Unwrapping error correction and noise reduction. Computers & Geosciences, 133, 104331. https://doi.org/10.1016/j.cageo.2019.104331

Zhang, Z., Lin, H., Wang, M., Liu, X., Chen, Q., Wang, C., & Zhang, H. (2022). A Review of Satellite Synthetic Aperture Radar Interferometry Applications in Permafrost Regions: Current status, challenges, and trends. IEEE Geoscience and Remote Sensing Magazine, 10(3), 93–114. https://doi.org/10.1109/MGRS.2022.3170350

Zheng, W., Bhushan, S., Van Wyk De Vries, M., Kochtitzky, W., Shean, D., Copland, L., Dow, C., Jones-Ivey, R., & Pérez, F. (2023). GLAcier Feature Tracking testkit (GLAFT): A statistically and physically based framework for evaluating glacier velocity products derived from optical satellite image feature tracking. The Cryosphere, 17(9), 4063–4078. https://doi.org/10.5194/tc-17-4063-2023